HOSTED BY
ELSEVIER
Available online at www.sciencedirect.com
ScienceDirect
Soils and Foundations 61 (2021) 1581–1596
www.elsevier.com/locate/sandf

Technical Paper

Testing and modelling total suction effects on compressibility and creep of crushable granular material

Rodrigo Osses [a,b], Kasra Majdanishabestari [c,d], Carlos Ovalle [c,d,*], Jubert Pineda [e]

[a] Facultad de Ingeniería y Ciencias, Universidad de La Frontera, Chile
[b] Dept. of Structural and Geotechnical Engineering, Pontificia Universidad Católica de Chile, Chile
[c] Research Institute of Mining and Environment (RIME UQAT-Polytechnique), Canada
[d] Dep. of Civil, Geological and Mining Engineering, Polytechnique Montréal, Québec, Canada
[e] University of Newcastle, Faculty of Engineering and Build Environment, Australia

Received 1 July 2020; received in revised form 28 July 2021; accepted 22 September 2021
Available online 11 October 2021

Abstract

Recent works have shown that delayed events of particle crushing are partially responsible of creep deformation in granular materials, and that Stress Corrosion Cracking promoted by high humidity within particles is the source of this mechanism. A number of experimental studies have focused on creep behaviour of water saturated samples and wetting-deformation after soaking dry material. However, there are few evidences of the effect of varying total suction in time-dependent deformation of partially saturated crushable material, and this mechanism have been rarely considered in constitutive models. The aims of this paper are to present experimental evidence of the effect of total suction on compressibility and creep of sandy sized samples from crushed rock, and to propose a simple one-dimensional elasto-plastic modelling approach based on the enhancement of an existing model. Oedometric compression tests at different total suctions are presented. The results show that compressibility and creep strains increase with both stress and humidity. The model proposed uses a time-dependent hardening law coupling suction with the amount of particle breakage. Based on preliminary calibrations, the model captures the effect of suction and time-dependent behaviour over a large range of total suction.

Keywords: Particle breakage; Partial saturation; Creep; Constitutive modelling

1. Introduction

Time-dependent deformation in crushable granular materials has been monitored in diverse geotechnical structures such as rockfill dams (Parkin, 1991; Alonso et al., 2005), railway ballast (Indraratna et al., 2011), piles (Leung et al., 2011), surface subsidence of deep reservoirs (Brzesowsky et al., 2014), slip stability of fault gouges (Main and Meredith, 1991), among others. Although these observations have motivated a number of experimental studies (Sowers et al., 1965; Lee and Farhoomand, 1967; Nobari and Duncan, 1972; Lee and Coop, 1995; Ovalle et al., 2013), this phenomenon has been rarely incorporated in constitutive models for crushable granular materials.

Based on the pioneering work of Scholz (1968), who stated that creep in brittle rocks is due to time-dependent cracking, a number of geotechnical researchers have hypothesized that creep in granular materials (i.e. secondary compression upon constant loading) is mainly due to particle breakage evolving in time (e.g., Oldecop & Alonso, 2001; Lade and Karimpour, 2010; Ovalle et al., 2015; Sohn and Buscarnera, 2019). This approach is supported experimentally by particle size distribution

Peer review under responsibility of The Japanese Geotechnical Society.
* Corresponding author at: Polytechnique Montréal (Room A-356), 2900 Edouard Montpetit Blvd, Montreal, QC H3T 1J4, Canada.
E-mail address: carlos.ovalle@polymtl.ca (C. Ovalle).

https://doi.org/10.1016/j.sandf.2021.09.006
0038-0806/

(PSD) analyses before and after loading tests. For instance, Takei et al. (2001) reported observations of time-dependent crushing on 2D granular samples composed by chalk and talc cylinder bars, showing that late crushing events at the grain scale are predominantly responsible for creep strains at the macro-mechanical scale. Recently, Andò et al. (2019) gave strong support to this statement, reporting X-ray tomography observations of delayed grain fragmentation events during creep tests on sand.

A number of experimental studies on granular soils have focused on creep behaviour after wetting-deformation due to soaking (Sowers et al., 1965; Lee and Farhoomand, 1967; Nobari and Duncan, 1972; Marsal, 1973; Lee and Coop, 1995; Brzesowsky et al., 2014; Chen et al., 2020). However, only few works have reported the effect of partial saturation over a wide range of total suction (Oldecop and Alonso, 2001, 2004; Chávez and Alonso, 2003; Alonso et al., 2016; Osses et al., 2019), despite its importance for the development and calibration of constitutive models for partially saturated crushable materials.

Elasto-plastic constitutive models for crushable soils typically include breakage-dependency on critical void ratio and/or hardening variables (Daouadji et al., 2001; Muir Wood et al., 2009; Kikumoto et al., 2010; Daouadji and Hicher, 2010; Hu et al., 2011; Xiao and Liu, 2017; Yin et al., 2017; Ovalle and Hicher, 2020). However, few attempts have been made to model creep in crushable materials. Among these works, Oldecop and Alonso (2007) settled a conceptual model based on Stress Corrosion Cracking (SCC) concept, Bauer (2009) proposed a hypoplastic model with time-dependent solid hardness, and recently Zhang and Buscarnera (2017) developed a thermomechanical model incorporating rate-effects according to SCC. Nevertheless, further developments are still required to include creep behaviour of crushable granular materials within mathematical frameworks such as elasto-plasticity, aimed at improving the reliability of geotechnical predictions for rockfill materials. Fu et al. (2019) presented a recent approach in this sense, however, since particle breakage is responsible of a significant part of creep deformation, physical based modelling approaches should be also focused on time-dependent breakage.

This paper has two main objectives: (1) to present experimental evidence of the effect of total suction on compressibility and creep of sandy sized samples from crushed rock, and (2) to propose a simple one-dimensional compression elasto-plastic constitutive model considering particle breakage and creep deformation. A series of oedometric compression tests on partially saturated sandy soil from crushed rock are presented. In these tests, total suction was imposed during one-dimensional compression by controlling the relative humidity of the air in contact with the specimens via the vapour transfer technique. The range of total suction applied varies from 0 (fully saturated conditions) to 340 MPa. The results are used to calibrate a time-dependent hardening law for one-dimensional compression modelling, coupling the amount of particle breakage with suction in order to model compressibility and creep.

2. Stress corrosion cracking and relative humidity effects in granular geomaterials

Oldecop and Alonso (2001, 2007) postulated that creep settlements generated by delayed events of particle crushing are caused by the phenomenon of SCC (Atkinson, 1984), occurring at pre-existing cracks (intraparticle microcracks) within grains. According to the SCC concept, crack tips in stressed grains are slowly corroded by water or humid environments, increasing crack growth velocity and thus triggering deferred fragmentation. The chemical action of water can be evaluated in terms of the relative humidity (RH) of the air in contact with grains. The effect of the RH on crack propagation velocity is commonly expressed through the following general expression (Freiman, 1984; Atkinson and Meredith, 1987; Oldecop and Alonso, 2001):

$$V = V_0(RH)exp^{[(-E\ddagger+bk)/RT]} \quad (1)$$

where V is the crack propagation velocity, RH is the relative humidity of the air in contact with the tested material, k is the stress intensity factor in the crack, T is the absolute temperature, $R$is the gas constant and V_0, E‡ and b are constants estimated through fitting of experimental data.

On the other hand, when a specimen reaches equilibrium with the environment it has been exposed to, it is possible to estimate the total suction (ψ) generated by the surrounding RH using Kelvin's law (Fredlund & Rahardjo, 1993):

$$\psi = s + \pi = -\frac{RT}{v_{w0}\omega_v} ln(RH) \quad (2)$$

where s is the matric suction produced by capillary effects, π is the osmotic component of suction which considers the presence of solutes within the pore fluid, R is the universal gas constant (8.31432 J/[mol K]), v_{w0} is the specific volume of water, or the inverse of the water mass density ($1/\rho_w$ m^3/kg) and ω_v is the molecular mass of the water vapour (18.016 kg/mol). In cases where the presence of solutes within the pore fluid is negligible, the osmotic component of suction is not considered and therefore the total suction is assumed to be controlled by capillary effects acting at intraparticle and interparticle levels.

Therefore, the humidity that matters for the SCC phenomena to occur is that inside intraparticle cracks, which can be managed by controlling the air RH of interparticle voids using the vapour transfer technique (Blatz et al., 2008), where target RHs are produced using saline solutions. According to Eq. (2), unsaturated conditions covering a large range of total suction can be reached by controlling constant RH in a system where liquid and gas phases are at equilibrium. When a specimen is exposed to a change in RH within a closed system, water transfer takes place through the vapour phase by pure diffusion or advection until equilibrium is achieved. The specimen will absorb water if the RH within particles (intraparticle voids) is

lower than the RH of interparticle voids. Upon wetting, water vapour will condensate inside small pores but also at contact points between particles, reducing suction generated by surface tension at the air/water interface and, at the same time, accelerating the propagation of microcracks within particles. Upon drying, the low RH of the vapour phase will promote a release of moisture and water could remain within intraparticle cracks (Fig. 1), thus delaying crack corrosion according to Eq. (1). The most favourable condition for SCC will occur at RH = 100%, which also means that ψ vanishes in Eq. (2); theoretically this condition can be achieved under fully water saturated condition.

3. Laboratory program

3.1. Material tested and sample preparation

The material was collected from a quarry near the town of Colina in the Metropolitan Region of Chile. This rock is often used as dyke construction material and railway ballast, as well as decorative purposes. It corresponds to Andesite, an extrusive rock belonging to the Volcanic Group of the Oligo-Miocene era. Characteristic crystalline mineral phases of the material were identified with X-ray diffraction (XRD) using a powder diffractometry (D2 Phaser, Bruker AXS, Germany) at 30 kV and 10 mA using Cu-K(alpha) radiation. XRD analysis confirms that the main components are silica in the form of Quartz and feldspar in the form of Anorthite, which is expected in Andesite igneous rocks.

Tests presented in this paper were carried-out on sandy sized samples taken from the Andesite Colina crushed rock, constituted by the size fraction from 1.18 to 2 mm, and classifying as poor graded sand (SP) according to the Unified Soil Classification System. Table 1 includes index properties while Fig. 2 presents the PSD of the material and illustrates the angular and flatty elongated shapes of the crushed particles, which should make them significantly vulnerable to breakage (Xiao et al., 2019; Ovalle and Dano, 2020).

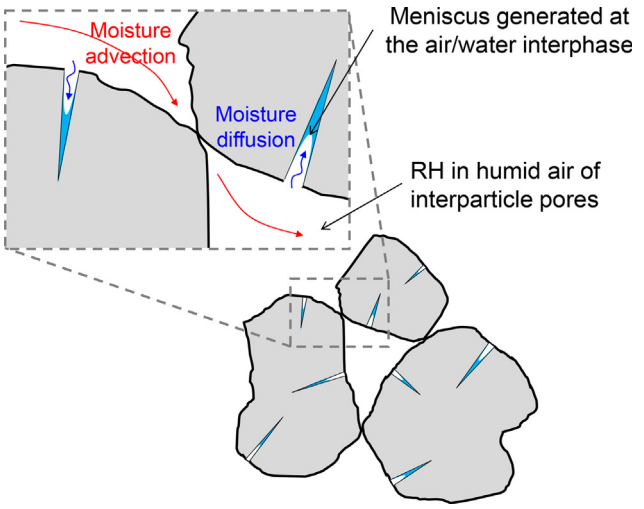

Fig. 1. Schematic unsaturated states of rock particles.

Table 1
Geotechnical parameters.

Group	Parameter	Value
Initial grading	d_{max}(mm)	2.00
	d_{min} (mm)	1.18
	C_u	1.3
Specific gravity	G_s	2.65
Relative density	e_{max}	1.258
	e_{min}	0.789

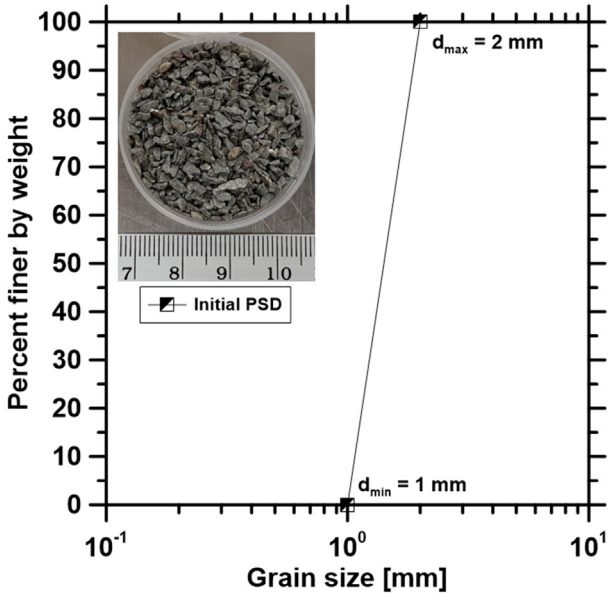

Fig. 2. Initial PSD of the sandy fraction of Colina crushed rock.

3.2. Water retention curve (WRC)

The WRC of the tested rock particles, defined in terms of the gravimetric water content ω (weight-based content) vs. ψ, was obtained by exposing specimens to controlled hydraulic paths using the vapour transfer technique. This was achieved by means of a closed air system in which the vapour mass remains constant and water vapour could be absorbed by rock particles. Note that, in order to study the effect of the material humidity on particle crushing and compressibility, according to the SCC concept the relevant values of ω are related to the intraparticle water storage capacity, in other words, humidity within microcracks of single crushed rock particles.

The estimation of the WRC followed a multi-stage approach. Starting from an unsaturated state, wetting (i.e. reduction in ψ) was achieved by exposing samples to water vapour for different lengths of time. To do so, cylindrical specimens were placed into sealed containers partially filled with deionized water which produces a RH ≈ 98% (see Fig. 3). When target values of water content

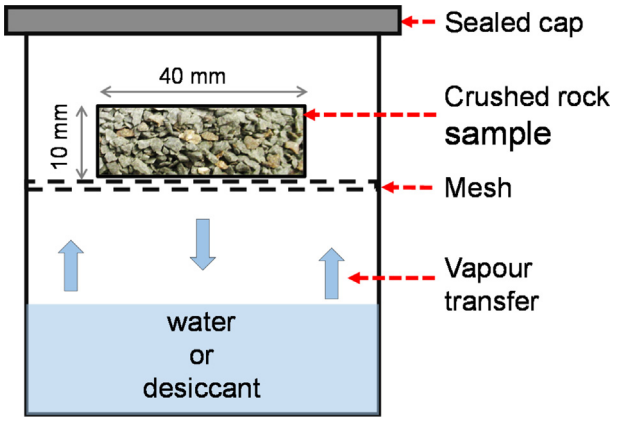

Fig. 3. Scheme of the sealed container for controlling the RH via the vapour transfer technique on cylindrical samples of sandy sized samples of Colina crushed rock.

change are reached, the samples were extracted, sealed and stored at controlled conditions for at least 48 h to allow them to reach suction equilibrium prior weighting and measuring the total suction using the WP4C dew-point psycrometer (Decagon Devices®, 2018). This device measures the temperature at which condensation first appears (dew-point temperature) when a sample reaches equilibrium with the surrounding air within the housing chamber. Each measurement of total suction with the WP4C psycrometer took around 15 min. Drying was applied by exposing the samples to a RH≈15% (using silica desiccant beads into the sealed containers, see Fig. 3) until a target water content was achieved. The same equalization period (48 h) was adopted during the drying path prior measuring total suction with the WP4C psycrometer. The aforementioned process was repeated until measured suction was close to the upper (300 MPa) and lower (0.05 MPa) limits of the WP4C device.

Fig. 4 presents the wetting and drying branches of the WRC obtained from two identical samples. Experimental

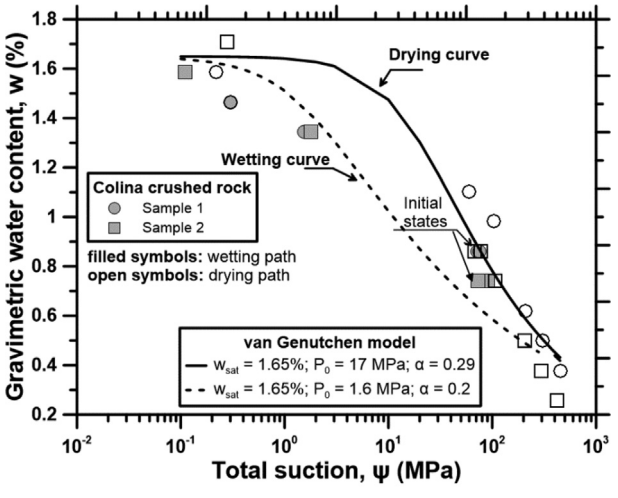

Fig. 4. Water retention curve.

results have been fitted using the van Genuchten-type model proposed by Jacinto et al. (2009):

$$\omega = \omega_{sat}\left[1+\left(\frac{\psi}{P_0}\right)^{\frac{1}{1-\alpha}}\right]^{-\alpha} \quad (3)$$

where ω_{sat} is the gravimetric water content at saturated conditions, and P_0 and α are fitted parameters shown in Fig. 4 for wetting and drying paths. A value of $\omega_{sat} = 1.65\%$ was fitted and the results indicate that ω of the crushed rock particles for total suction of 340 MPa is around 0.3%. These values are consistent with the fact that water storage capacity of crushed rock materials is mainly controlled by intraparticle voids, and are in a similar range compared to slate crushed rock particles tested by Oldecop & Alonso (2001) and waste rock particles from iron mining reported by Osses et al. (2019). Note that the range of ω from 0.3 to 1.65% results in very low degrees of saturation of 1–5%, respectively (i.e. ratio of volume of water and volume of interparticle voids), because water is being stored in microscopic volumes of intraparticle cracks, while interparticle voids remain filled with humid air. However, such low changes of ω could lead to significant variations on particle breakage and creep (Oldecop & Alonso, 2004). Therefore, to characterize the material state reflecting the effect of humidity on intraparticle cracks it is more appropriate to use ψ (Oldecop & Alonso, 2001; Alonso et al., 2016), which varies over a large range up to 340 MPa in this study.

3.3. Oedometric compression tests

Samples for oedometric compression tests were prepared by dry tamping using two layers of 10 mm in height, targeting a relative density of 80% (i.e. void ratio of e =0.883). Oedometer tests were performed in a stainless-steel cell of 63 mm in diameter and 20 mm in height. The high initial relative density chosen to avoid possible scattering in the initial density of loose samples, eventually caused by densification due to slight disturbance during sample preparation and during installation in the oedometer apparatus. Some samples were dismantled after preparation with the aim of checking if particle breakage could take place during preparation. The results indicated that the initial PSDs were unchanged when compared with the material after sample preparation and after e_{max} and e_{min} testing.

Compression tests were performed by applying vertical stress increments to a standard double drainage oedometric cell installed in a classical front-loading frame. The following vertical stress increments were applied: 10, 25, 50, 100, 200, 400, 800 and 1600 kPa. Each increment was maintained for 24 h and the higher value corresponds to the maximum loading capacity of the apparatus. In order to control the RH within the compressed samples, we used the vapour transfer technique and ψ was calculated using Eq. (2) with the measured values of air RH at equilibrium in the closed system described hereafter.

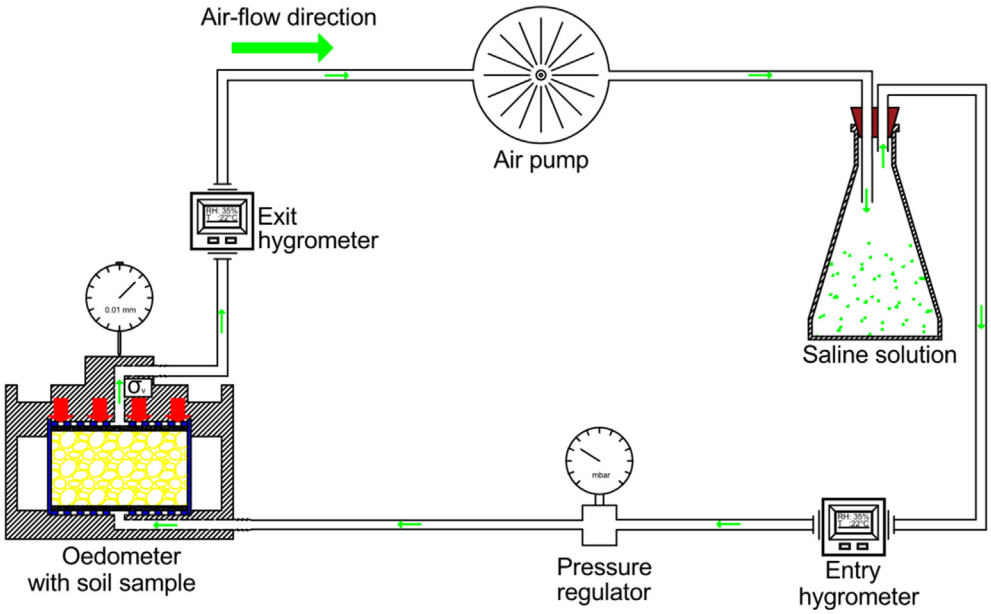

Fig. 5. Air flow system for vapour control in the oedometric test.

A forced-convection system composed of an air pump connected to a vessel with saline solution and to the top and bottom drainage lines of the oedometer cell was designed and implemented to circulate water vapour through the specimen (see Fig. 5). To avoid modifications in the target RH, a pressure regulator was installed to maintain the air pressure generated by the pump at a constant low value of 2 kPa. In this system, two hygrometers monitor temperature and RH within the closed loop. Following the air flow direction, the first hygrometer controls the RH of the air before entering the sample, and the second one measures the RH of the air after passing through the specimen and been recirculated to the vessel containing the saline solution. According to existing correlations between chemical compositions of salts and RH at equilibrium (Romero, 2001), different saline solutions were used in order to cover a wide range of RH from 9 to 95%, as presented in Table 2, where ω after equilibrium was estimated from the WRC presented in Fig. 4. The vessel contained saturated saline solutions, except for the driest test, where a dry NaOH salt was placed in the vessel to reach an average value of RH = 9%.

Each test was carried-out under constant RH. Before applying the first load increment, an equalization period was allowed in the air loop containing sample in the oedometer cell, in order to achieve the stabilisation of the air humidity within the closed system by recording a constant RH in the hygrometers; this period was of 2–3 days, depending on the final value of RH. Once RH was stable, additional 3 days of equalisation were allowed to ensure that the system could maintain stable conditions. Then, the vertical stress increments were applied during 8 successive days (i.e. 24 h of constant stress for each increment). Finally, the unloading stage was completed in 4 successive days. Fig. 6 illustrates that RH recorded was reasonably stable during 15 days of testing for each sample (3 days

Table 2
Experimental tests.

Test ID	Initial void ratio, e_0 (1)	Saturated saline solution	Average RH (%)	Total suction, ψ (MPa)	Gravimetric water content, ω(%) (4)	Particle breakage index, B_r (%)	Plastic work, w_p (MPa)	C_α/C_c
340	0.880	NaOH (2)	9	340	0.48	–	0.0347	0.0227
260	0.879	KOH	15	260	0.68	1.8	0.0385	0.0256
130	0.881	$MgCl_2$	39	130	0.58	2.4	0.0399	0.0255
70	0.878	NaOH	66	70	0.64	3.7	0.0422	0.0277
70r	0.884	NaBr	66	70	0.64	2.8	0.0354	0.0254
10	0.881	K_2SO_4	93	10	0.90	4.4	0.0498	0.0351
0	0.877	(3)		0	33.3	4.8	0.0568	0.0437
0r	0.882	(3)		0	33.3	4.0	0.0669	0.0313

(1) target value:$e_0 = 0.883$.
(2) dry salt, all the rest were saturated solutions.
(3) samples saturated with demineralized water.
(4) ω after RH equalisation for unsaturated tests and after soaking for fully saturated.

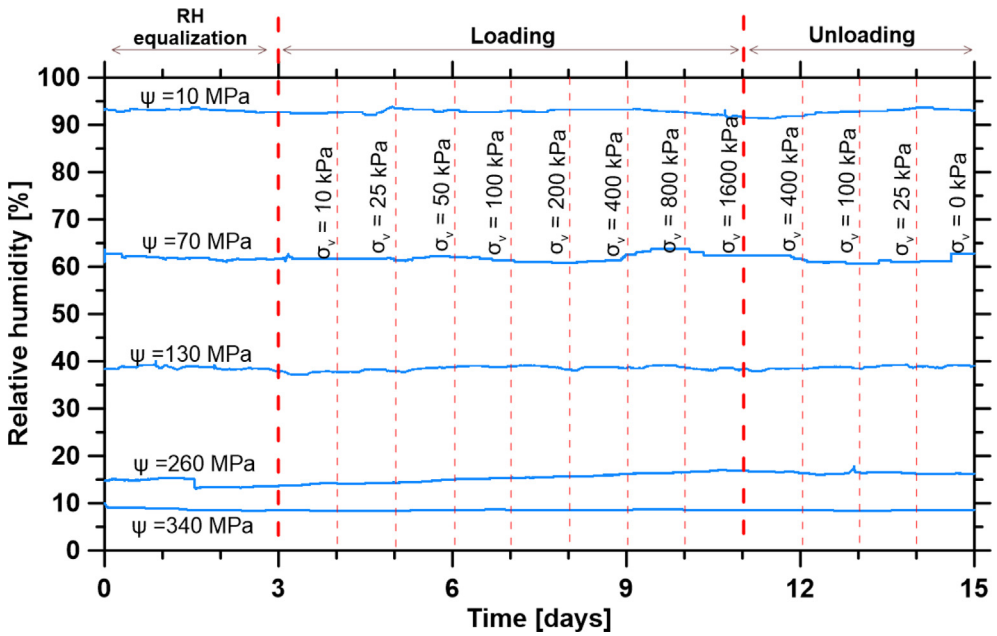

Fig. 6. Monitored RH during 15 days of testing.

of RH equalisation +8 days of loading +4 days of unloading), where total suctions were obtained according to Eq. (2).

Two samples were also tested under fully water saturated conditions (i.e. $\psi = 0$) using demineralized water (see Table 2). This condition ensures that there is no matric suction acting on interparticle contacts, therefore the results are comparable with the samples tested under total suction control (i.e. controlling intraparticle ψ through RH and Eq. (2)), where interparticle pores have no liquid water affecting the effective stress state due to capillary effects. Specimens were soaked with demineralized water and an equalization period of 3 days was allowed before loading. The same stress path as for the rest of the tests was applied (i.e. 24 h for each increment).

3.4. Experimental results and discussion

Fig. 7 shows the compressibility curves ($e - \log\sigma_v$) for eight one-dimensional compression tests carried out at different total suctions. The repeatability of the tests was checked for water saturated conditions ($\psi = 0$) and total suction of 70 MPa (tests 0r and 70r in Fig. 7 and Table 2). Overall, Fig. 7 shows an increase in compressibility with decreasing total suction. Nevertheless, this effect is less discernible for total suctions $\psi \geq 70$ MPa where the moisture content estimated from Fig. 4 is less than 0.7%. The magnitude of this suction limit ($\psi = 70$ MPa for the current case), where only low changes in compressibility are obtained under drier conditions, will strongly depend on the water retention properties of the material; for instance, it could occur at higher ψ in a material with thinner microcracks. Fig. 8 presents the final PSD estimated after testing, confirming that particle breakage increases with decreasing total suction, which is consistent with the SCC concept. In other words, increasing intraparticle humidity (or RH) promote crack corrosion as indicated by Eq. (1). Thus, finer particles are created by grain fragmentation and the material reaches a denser condition for a given stress level, when compared with a drier sample. It is worth noting that, even if fully saturated tests are the most compressible, their final PSDs are similar to the one for the specimen tested at $\psi = 10$ MPa. This is probably due to water acting as lubricant at inter-particle contacts, contributing to increased

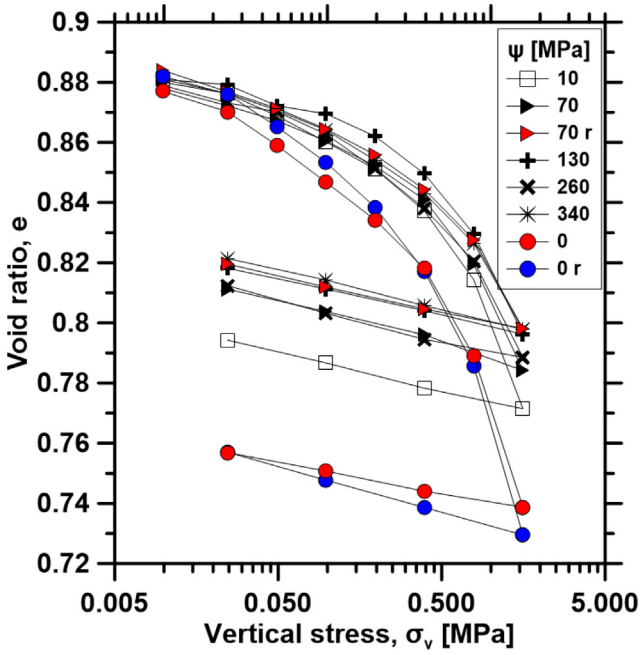

Fig. 7. Oedometric compression curves.

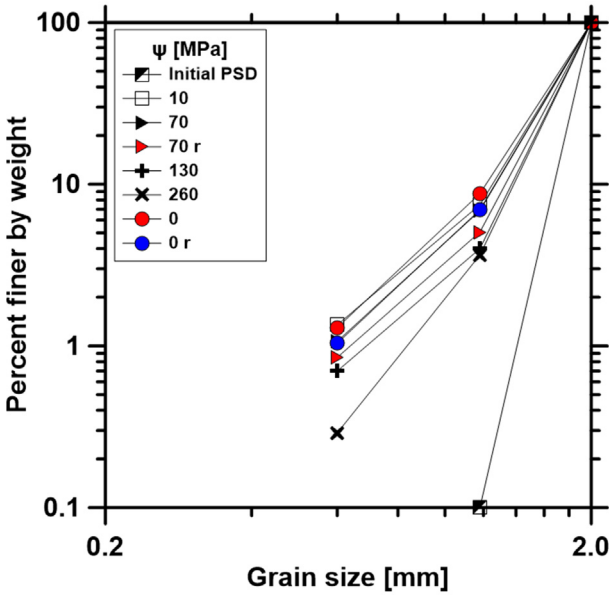

Fig. 8. Particle size distributions before and after oedometric testing.

compressibility by enabling particles sliding and rearrangement (Xu et al., 2007).

Fig. 9 shows time-deformation data recorded for different loading steps for specimens equilibrated at total suctions of $\psi = 0$, 70 and 340 MPa. This figure can be used to estimate the secondary compression index $C_\alpha = -\Delta e/\Delta \log t$ for each loading step. The results indicate that C_α can be estimated after 0.1 min irrespective of the stress level applied and reveals that, after a short period of time (here of 0.1 min), the deformation mechanism is mainly due to secondary compression. This behaviour is in agreement with the high hydraulic conductivity expected for the clean sand tested in this research, which should be in the range of 0.1–0.5 cm/s since the material classifies as uniform sand without fines (Lambe and Whitman, 1969; West, 1995). Thus, it is reasonable to assume that primary consolidation is achieved within the first seconds after loading. Similar behaviour was obtained in previous works on granular uniformly graded samples without fines, such as rockfill (Oldecop and Alonso, 2007), sand fraction of crushed rock (Ovalle et al., 2015) and quartz sands (including round Ottawa quartz sand) (Sohn and Buscarnera, 2019), where the authors also assumed that the time-lapse for primary consolidation was negligible. Therefore, in this study C_α values were calculated between 0.1 and 1440 min.

It could be expected that if constant vertical stress is maintained for additional time (>24 h), more particle crushing events should produce more creep strains, eventually slightly altering the compressibility curve. However, empirical evidence shows that the PSD evolves to an ultimate state under very high plastic work (Turcotte, 1986; Nakata et al., 2001; Coop et al., 2004), where crushing and creep strains should stop. Nevertheless, there is no experimental evidence of such an ultimate state under creep of crushable granular materials and, according to the low changes of the PSD produced by creep in 24 h (Sohn and Buscarnera, 2019), it seems that an ultimate state should require a significant amount of time to be achieved. This could explain why rockfill dams continue to settle after

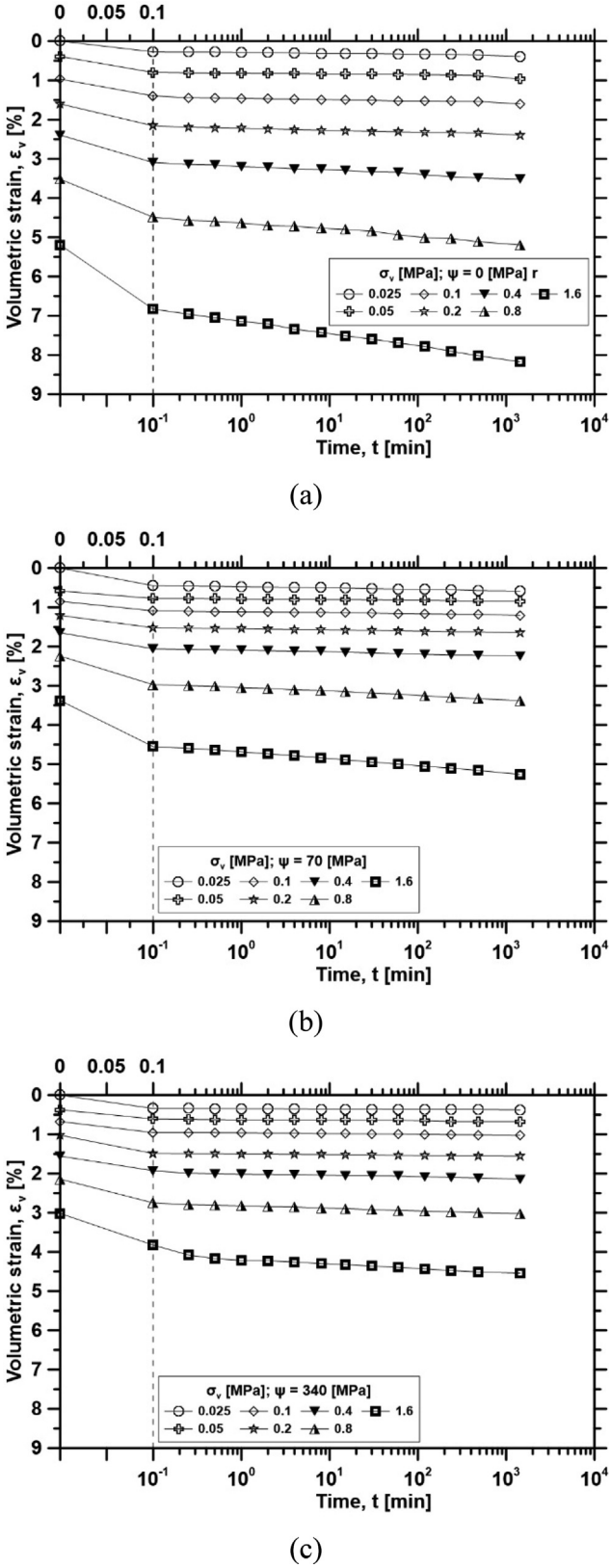

Fig. 9. Time-settlement for tests at (a) $\psi = 0$ MPa, (b) 70 MPa and (c) 340 MPa.

more than 40 years of construction (Parkin, 1991; Alonso et al., 2005).

Fig. 10 presents the compression index $C_c = -\Delta e/\Delta \log \sigma_v$ and C_α for each stress increment in all tests. Despite of some scatter observed at low stress levels, a clear trend is observed at high stresses, where C_c and C_α increase with vertical stress and RH (reduction in ψ). The effect of ψ on C_c is evident when comparing the compression curve of the test at ψ =10 MPa with less compressible drier tests at $\psi \geq 70$ MPa. As expected, tests at ψ =0 MPa shows the higher C_c. Increasing C_α with decreasing total suction agrees with the hypothesis that creep is promoted in humid environments, due to both higher corrosion and crack growth velocity.

Fig. 11a shows the ratio C_α/C_c for all the tests presented in this paper. The C_α/C_c concept proposed by Mesri and Godlewski (1977) has great importance in soil compressibility because it defines secondary compression behaviour of any soil in terms of a constant C_α/C_c ratio (see also Mesri and Castro, 1987). The concept is based on the

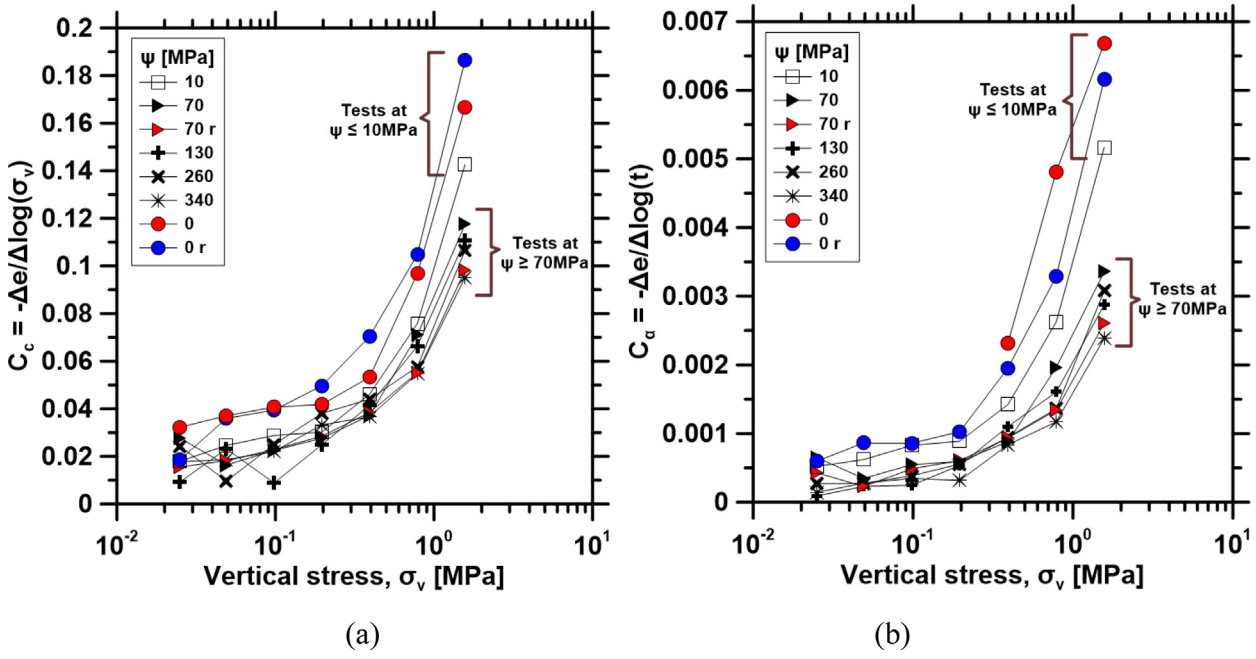

Fig. 10. Indexes for (a) total and (b) secondary compression.

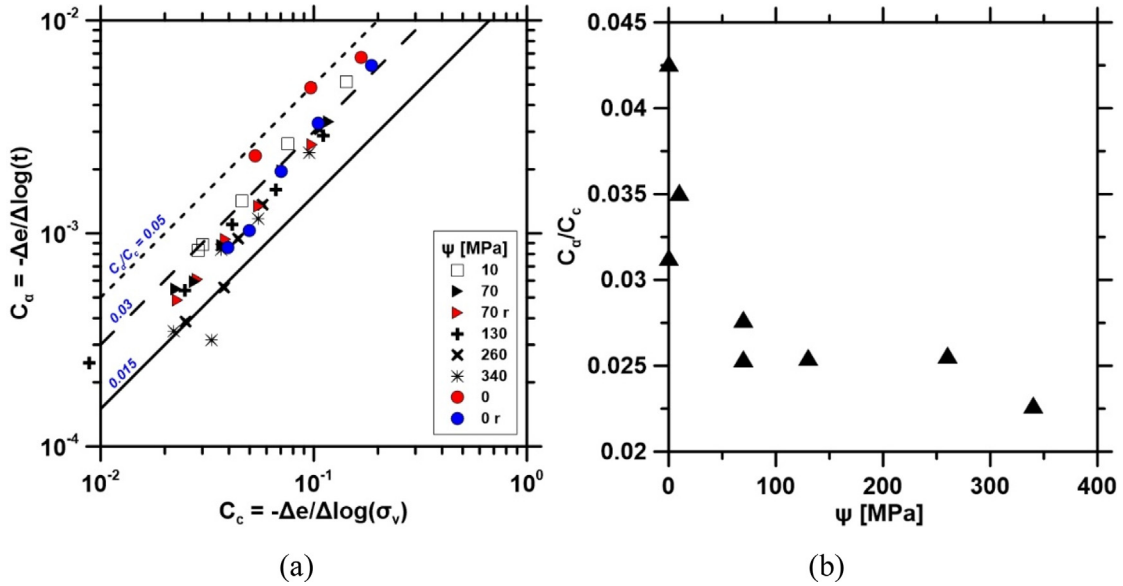

Fig. 11. Compressibility index ratio: (a) all tests and stress increments and (b) best fitting for C_α/C_c at each total suction.

empirical observation that the magnitude of C_α ant its evolution with time is directly related to the magnitude of C_c and its variation with vertical stress under oedometric compression. For this study, Fig. 11a confirmed that a constant C_α/C_c can be observed for the material tested at a given ψ. Moreover, it can be observed that tests at $\psi \geq 70$ MPa are within the range of C_α/C_c proposed by Mesri and Vardhanabhuti (2009) for crushable sands. However, tests at $\psi = 0$ and 10 MPa have slightly higher values of C_α/C_c, indicating that a threshold in the material behaviour might exists somewhere between ψ =10 and 70 MPa. This suggestion is consistent with the comparison of the set of C_c and C_α of all tests at $\psi \geq 70$ MPa, with tests at $\psi \leq 10$ MPa, as highlighted in Fig. 10. Fig. 11b indicates that C_α/C_c slightly decreases with suction, which agrees with previous studies on rockfill (Oldecop and Alonso, 2007) and crushable sand (Ovalle, 2018). Consequently, when ψ reduces (i.e. humidity increases), not only the magnitude of creep strains increases but also its contribution to total deformation.

It is worth noting that the results presented here could be highly dependent on grain characteristics, such as size, shape, hardness, and the degree of internal cracking related to their geological origin or induced damage in samples extraction (e.g. blasting and grinding). All these properties could strongly affect the material crushability, thus its stress–strain response. For instance, Oldecop and Alonso (2007) reported C_α/C_c values of 0.015 and less for "dry" slate rockfill under controlled RH, while Ovalle (2018) obtained values of 0.015 and 0.03 for the sandy fraction of "dry" and saturated quartzite shale rock, respectively. Therefore, while the results of C_α/C_c presented in this paper for $\psi \geq 70$ MPa are in agreement with reported data, the values obtained for $\psi \leq 10$ MPa appears relatively high, indicating that the material is sensitive to humidity.

Fig. 12 illustrates the swelling index $C_s = -\Delta e/\Delta \log \sigma_v$ over the unloading paths of Fig. 7. It can be concluded that

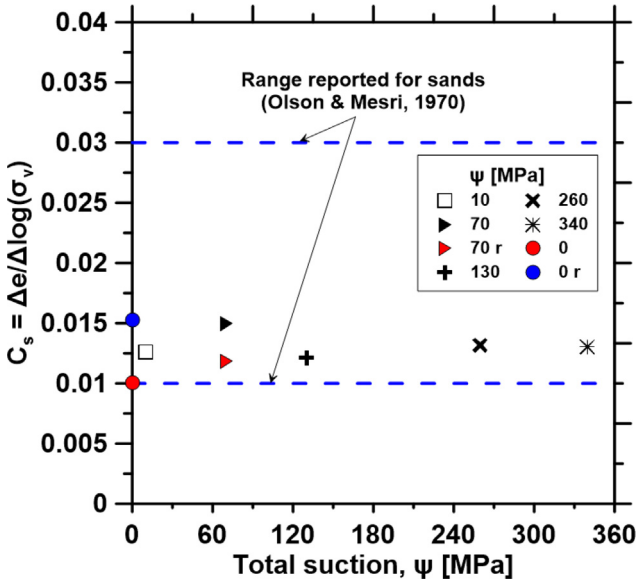

Fig. 12. Swelling indexes.

C_s does not depend on total suction, and the results are in a short range of 0.01–0.015, which is consistent with the range of 0.01–0.03 reported by Mesri and Vardhanabhuti (2009) for several crushable sands. The experimental evidence presented above indicates that a single set of elastic parameters without suction dependency would be required to model the elastic behaviour of the tested rock.

4. Constitutive modelling

Experimental results described above remark the strong influence of total suction on particle breakage which, in turn, affects the compressibility and secondary compression behaviour of Colina crushed rock samples. In the following, a simple yet robust one-dimensional constitutive model for compression of granular material that considers the dependency of total suction on particle breakage, is described. The model, originally developed by Ovalle and Hicher (2020), is extended here to take into account secondary compression behaviour. The experimental results described above are used to calibrate the model and to highlight important features of the material behaviour.

4.1. Coupling particle breakage and plastic work

In order to couple the effect of particle breakage with the stress–strain response of crushable samples, Ovalle and Hicher (2020) proposed the following relationship linking the particle breakage index (B_r) with the plastic work (w_p):

$$B_r = \left(\frac{w_p}{a + w_p}\right)^c \tag{4}$$

where a is a material constant, c depends on the wetting condition, and the plastic work is computed as

$$\mathrm{w_p} = \int \left(p d\varepsilon_v^p + q d\varepsilon_d^p\right) \tag{5}$$

where $d\varepsilon_v^p$ and $d\varepsilon_d^p$ are the volumetric and deviatoric plastic strain increments, respectively, p is the mean stress and q is the deviatoric stress. The definition of Einav (2007) was adopted for $B_r = B_t/B_p$, where B_t is the area flanked by the initial PSD and any intermediate PSD after crushing, and B_p is the area flanked by the initial PSD and an assumed ultimate fractal distribution. In fact, empirical data indicate that the PSD in granular materials subjected to high plastic work (i.e. high stress and/or large strains) evolves to an ultimate fractal distribution (Turcotte, 1986), that can be written in percent passing by weight as

$$F_u(d) = (d/d_{max})^{3-D} \tag{6}$$

where the exponent D is called the fractal dimension, d is the particle size and d_{max} is the size of the coarsest grain. According to extensive experimental data (Turcotte, 1986; Nakata el al., 2001; Coop et al., 2004), the exponent Dtends asymptotically to around 2.5–2.7 in crushable materials subjected to high plastic work. Therefore,

$B_r = 0$ for no crushing, and $B_r = 1$ when the ultimate fractal distribution is reached. Thereafter, $D = 2.5$ is assumed for modelling.

Other authors have proposed the relationship in Eq. (4) using only the material parameter a (i.e. with $c = 1$), showing that it is valid for values up to more than $w_p = 10$ (MPa) (Hu et al., 2018; Dano et al., 2018). As presented in Fig. 13a, schematic plots of Eq. (4) indicate that c defines the onset of crushing and a controls the shape of the relationship. Ovalle and Hicher (2020) have shown that, for a given material, Eq. (4) does not depend on the stress path, but only on the wetting condition. Therefore, providing calibration for a, c could be fitted for a given partially saturated condition. This finding suggests that Eq. (4) can be introduced into a constitutive model in order to couple the stress–strain response with the evolution of particle breakage along any stress path, and the effect of partial saturation could be captured by a total suction-dependent expression for c. As shown in Fig. 14 for all the tests presented in this study, B_r varies non-linearly with ψ, and tends to stabilize at its highest level of 4 to 5% at low ψ,

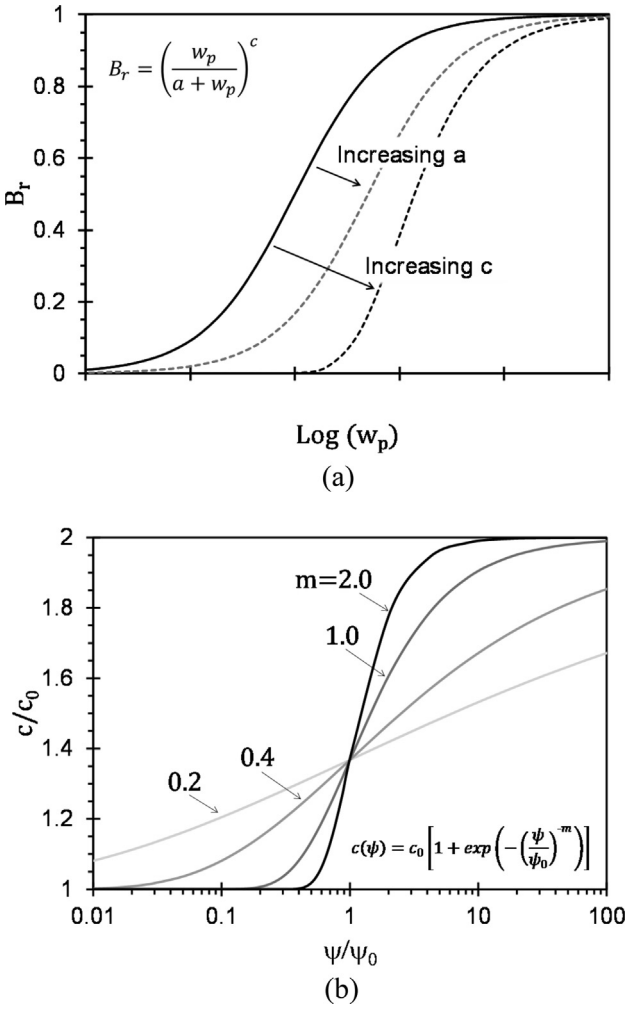

Fig. 13. Coupling particle breakage B_r, w_p and ψ: (a) effect of parameters a and c, and (b) shape of the suction dependent c-function.

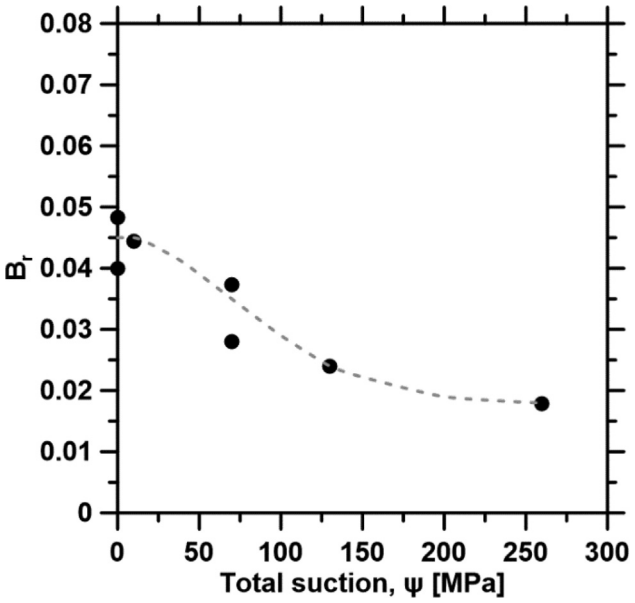

Fig. 14. Particle breakage index B_r against ψ.

and at its lower value at high ψ (B_r 2%). This behaviour is consistent with the SCC concept, which states that, a given stress state, higher amounts of particle breakage should occur in humid materials. Therefore, since the effect of increasing c is shifting the $B_r - w_p$ curve towards higher values of w_p, the effect of total suction on particle breakage could be captured by a direct relationship between c and ψ (i.e. the higher ψ, the higher c), provided that c tends to steady values at high and low levels of ψ (i.e. an "S" shaped curve according to Fig. 14). For this kind of $c - \psi$ correlation, in this work we propose the following Weibull-type expression:

$$c(\psi) = c_0\left[1 + exp\left(-\left(\frac{\psi}{\psi_0}\right)^{-m}\right)\right] \tag{7}$$

where c_0 is a material parameter, ψ_0 is a reference total suction and $m > 0$ controls the shape of the function. Fig. 13b shows that Eq. (7) has double convexity for logarithmic evolution of ψ, allowing for asymptotic values in both low and high suction values. Thus, the effect of suction tends to stabilize at $c/c_0 = 2$ for high ψ, and at a higher value of $c/c_0 = 1$ for low ψ. It is also clear that the lower the value of m, the smoother the variation of c (thus also in crushability) for a range of suctions around ψ_0.

From the experimental data presented in this paper, the tests at ψ =10 and 260 MPa were chosen for calibration of Eqs. (4) and (7) shown in Fig. 15. As discussed before, ψ_0=70 MPa can be set as an intermediate value within the range of ψ tested, allowing for a transition in accordance with the experimental data; namely, slight differences in compressibility for tests at ψ >70 MPa, and significant increasing of total and creep deformation at $\psi = 10$ MPa or less. Note that this calibration is limited to low plastic work values and a given stress path, however, it is used

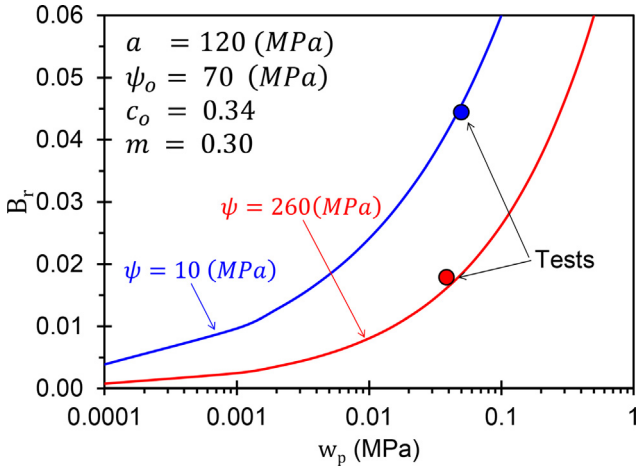

Fig. 15. Breakage and plastic work coupling calibration.

here only with the purpose of introducing the time-dependent elasto-plastic modelling approach.

4.2. Elasto-plastic formulation

Total strain increment is conventionally composed by elastic and plastic strain rates:

$$\dot{\varepsilon}_{ij} = \dot{\varepsilon}^e_{ij} + \dot{\varepsilon}^p_{ij} \tag{8}$$

Elastic strain increments ($\dot{\varepsilon}^e_{ij}$) are computed considering non-linear elasticity given by stress-dependent elastic bulk modulus (Richart et al., 1970):

$$K = K_0 \cdot p_{at} \frac{(2.97-e)^2}{(1+e)} \left(\frac{p}{p_{at}}\right)^n \tag{9}$$

where K_0 and n are material constants and $p_{at} = 101.3$kPa is the atmospheric pressure. Shear modulus G is obtained assuming a constant Poisson modulus (ν). Volumetric ($\dot{\varepsilon}^e_v$) and deviatoric ($\dot{\varepsilon}^e_d$) elastic strain increments are obtained as follows:

$$\dot{\varepsilon}^e_v = \frac{\dot{p}}{K} \quad \text{and} \quad \dot{\varepsilon}^e_d = \frac{\dot{q}}{3G} \tag{10}$$

The model of Ovalle and Hicher (2020) has an associate flow rule and considers the yield surface originally proposed by Kikumoto et al. (2010), later also adopted by Yin et al. (2017):

$$f = \frac{1}{2}\left(\frac{\eta}{M_p}\right)^3 p + p - p_m \tag{11}$$

where M_p is the stress ratio $\eta = q/p$ mobilized at the peak friction angle (ϕ_p), and p_m is the hardening function given by

$$p_m = p_{m_0} exp\left(\frac{1+e_o}{\lambda-\kappa}\varepsilon^p_v\right) exp(-bB_r) \tag{12}$$

and p_{m0} is the yielding pressure, e_o is the initial void ratio, λ is the compressibility index, κ is the swelling index ($\kappa = \lambda/10$ was adopted), and $b > 0$ is the rate of hardening due to particle breakage.

Plastic strain increments are computed as $\dot{\varepsilon}^p_{ij} = d\lambda(\partial f/\partial\sigma_{ij})$, where $d\lambda$ is given by the consistency condition:

$$\frac{\partial f}{\partial \sigma_{ij}}\dot{\sigma}_{ij} + \frac{\partial f}{\partial p_m}\cdot\frac{\partial p_m}{\partial \varepsilon^p_v}\left(d\lambda\frac{\partial f}{\partial p}\right) = 0 \tag{13}$$

For a given ε^p_v, p_m controls the yield surface expansion. At the same time, w_p increases and hardening is coupled with B_r according to Eq. (4). Therefore, to reach a given stress increment, p_m increases thanks to the term "$exp\left(\frac{1+e_o}{\lambda-\kappa}\varepsilon^p_v\right)$", and simultaneously decreases due to coupling in the term "$exp(-bB_r)$".

Based on this formulation, Ovalle and Hicher (2020) modelled flooding-collapse of crushable sand by simply using different values of b in Eq. (12); i.e. increasing its value in one order of magnitude to take into account wetting-collapse after soaking dry material at constant stress. In this paper, the effect of total suction is captured by Eq. (7), and time-dependent hardening for creep deformation is given by the following new expression for b:

$$b_i = b_{i-1} + \left(\frac{t_i}{t_{ref}}\right)^d \tag{14}$$

where i is the current stress increment, $d < 1$ is a material constant controlling the rate of creep, t_i is the time elapsed since the last stress increment, and t_{ref} is a reference time here equal to 0.1 min. The following modelling strategy for creep is schematically presented in Fig. 16:

a) Stress increment from A to B results in increasing plastic strains, thus increasing B_r through coupling with w_p.
b) After a first time-increment Δt, increasing b generates a reduction in p_m, which is compensated by additional creep strains to maintain constant stress at p_{m_B}.
c) Subsequent time increments repeat the latter effect, requiring additional creep strains until $p_m$convergence.

In summary, the model by Ovalle and Hicher (2020) has been extended in this work, through the implementation of two new equations: (i) Eq. (7) which considers the dependency of parameter c on ψ, and (ii) Eq. (14) which controls the time-dependent rate of breakage/hardening b.

4.3. Model calibration

The model was calibrated using the results from the test at $\psi = 10$ MPa. For the one-dimensional compression path, a constant ratio $\sigma_3/\sigma_1 = 0.5$ was adopted in the calculation of $p = (\sigma_1 + 2\sigma_3)/3$ and $q = \sigma_1 - \sigma_3$. Elastic moduli were fitted using the unloading path of the test, based on the relationships between oedometric modulus $E_{oed} = \Delta\sigma_1/\varepsilon_1$, Young modulus E and bulk modulus K:

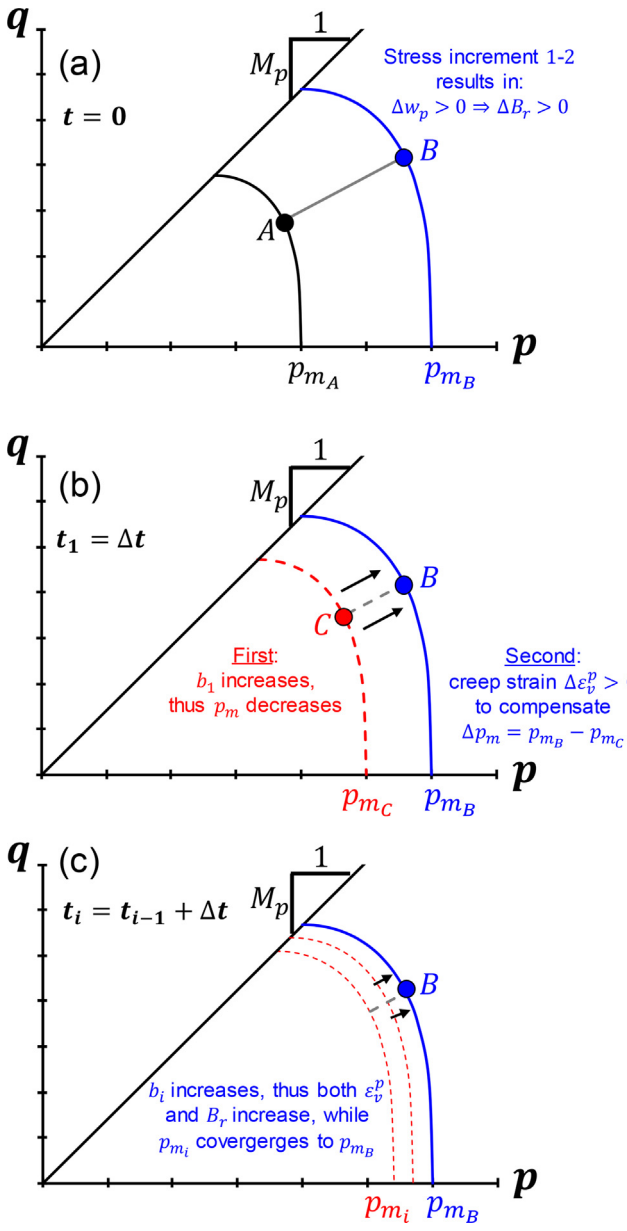

Fig. 16. Modelling strategy for time-dependent hardening during creep.

$$E = \frac{(1+v)(1-2v)}{(1-v)} E_{oed} \quad \& \quad K = \frac{E}{3(1-2v)} \tag{15}$$

According to empirical evidence of sands at 60% of relative density (Suwal and Kuwano, 2013), a constant Poisson's ratio $v = 0.25$ was assumed in Eq. (15). Fig. 17 illustrates the values of K computed from the unloading path of the test at $\psi = 10$ MPa (data of the tests at $\psi = 260$ MPa is also included for comparison). Based on a large data set for sands, Schanz and Vermeer (1998) reported values of n ranging from 0.4 to 0.8. Therefore, an intermediate value of $n = 0.6$ was first adopted in Eq. (9), in addition to $K_0 = 80$ and 150. As shown in Fig. 17, these values do not adequately represent the shape of the data, and a higher value of n is necessary. The best fitting

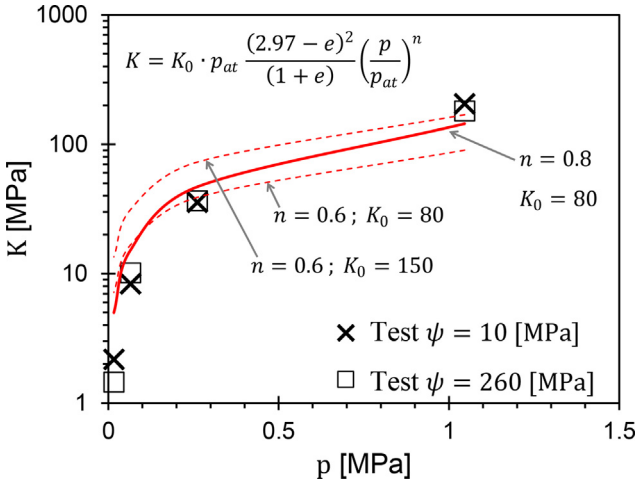

Fig. 17. Calibration of elastic parameters.

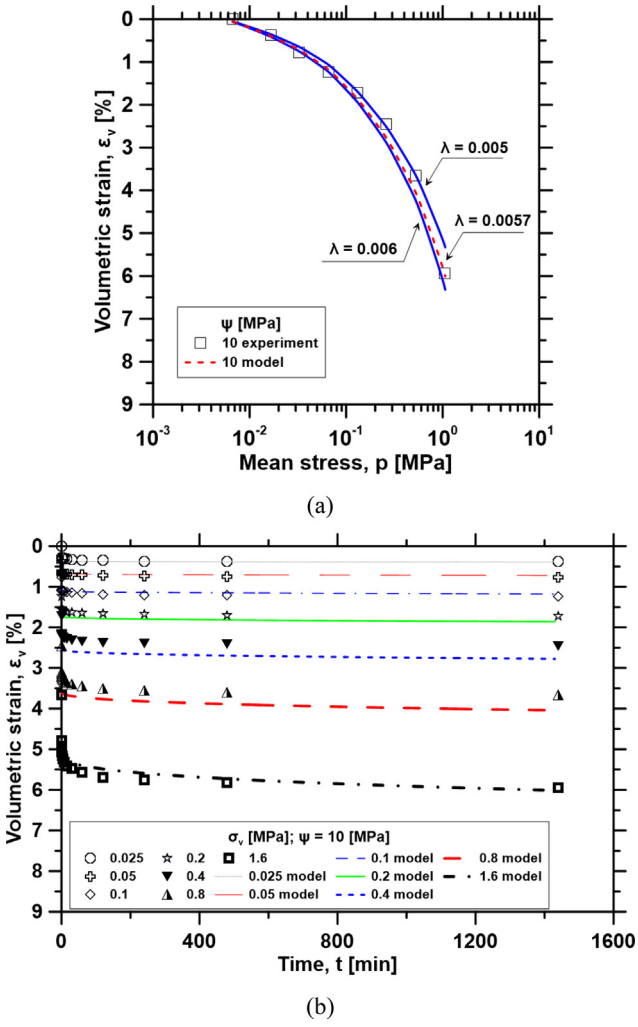

Fig. 18. Model calibration for test at $\psi = 10$ MPa: (a) compressibility for λ =0.005–0.006, (b) and time deformation for λ =0.0057.

of the experimental data was obtained by increasing n to 0.8 and using $K_0 = 80$. Although even higher values of n

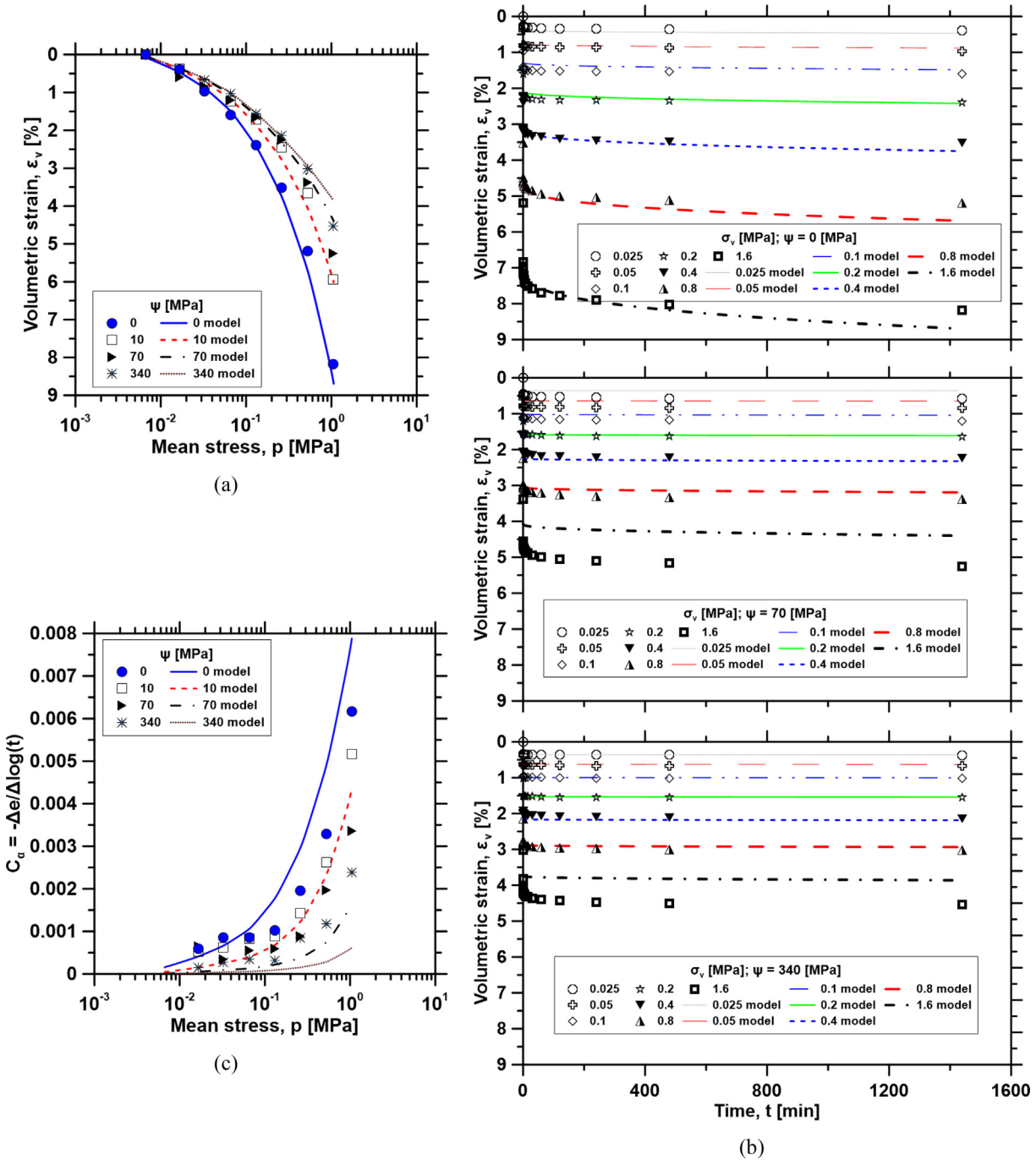

Fig. 19. Model simulations for tests at $\psi = 0$, 70 and 340 MPa: (a) compressibility, (b) time deformation and (c) secondary compression index.

could give a better adjustment, this option was discarded in order to fulfil the upper limit reported by Schanz and Vermeer (1998).

Provided that all samples show non-linear compression curves since the first stress increment and yielding pressure cannot be clearly observed, p_{m_0}=0.007 MPa (corresponding to the magnitude of the first stress increment $\sigma_v = 10$ kPa) was used for calibration and for all simulated cases. In other words, plastic strains are computed since the first stress increment applied in the tests. In the absence of shearing tests, a typical value of $M_p = 1.2$ was assumed, corresponding to a friction angle of $\phi_p = 30^\circ$ (according to the relationship $M_p = 6sin\phi_p/(3 - sin\phi_p)$). Finally, λ=0.0057 and $d = 0.37$ were calibrated to fit the test results at $\psi = 10$ MPa as presented in Fig. 18. There, simulations obtained for $\lambda = 0.005$ and 0.006 are also included for comparison and to support the choice of $\lambda = 0.0057$.

4.4. Model validation and discussion

The calibration of the test at $\psi = 10$ MPa presented in Fig. 18a confirms that the approach by Ovalle and

Hicher (2020), which consists in coupling particle breakage with plastic work within an elasto-plastic framework, is also suitable for the material tested in this study. Moreover, the new total suction-dependent relationship that controls the onset of particle crushing through the exponent c in the $B_r - w_p$ relationship successfully addresses the effect of ψ on crushed rock compressibility. This is presented in Fig. 19a for tests at $\psi = 0$, 10, 70 and 340 MPa. Simulations shown in this figure were obtained using the single set of parameters estimated from the calibration stage which are summarized in Table 3. It can be seen that the model is able to capture the main trend of the material behaviour, namely, increasing compressibility with both stress and total suction. Compression curves of tests at $\psi = 0$ and 10 MPa are accurately simulated over the whole range of vertical stress, while compressibility of tests at $\psi = 70$ and 340 MPa are well-captured until vertical stress of 0.8 MPa. The model underestimates the strains at stresses higher than 0.8 MPa, which is attributed here to the lack of data at high plastic work that should enhance the calibration of Eqs. (4) and (7) in that range, allowing for a better simulation of the response at high stresses.

In terms of creep strains, the simulations demonstrate that the implementation of a time-dependent rate of breakage hardening $b(t)$ is an adequate approach. Fig. 18b illustrates the simulations of time-deformation curves with very good agreement with the test used for calibration ($\psi = 10$ MPa). Fig. 19b presents simulations of creep strains for the tests used only for validation ($\psi = 0$, 70 and 340 MPa), again with good agreement for $\psi = 0$ MPa, as well as for $\psi = 70$ and 340 MPa until $\sigma_v = 0.8$ MPa. It is important to note that although the prediction of the secondary compression index C_α is a second order validation of the model, this is surprisingly well-reproduced for $\psi = 0$ and 10 MPa, while underpredicted for tests at $\psi = 70$ and 340 MPa. (see Fig. 19c).

Fig. 20 presents reasonable model assessments of B_r values compared to experimental data. It can be observed that the model overestimates B_r at low ψ, and underestimates it at high ψ. However, the model can capture the "S" shape of the relationship B_r vs. ψ. Note that the amounts of particle breakage at the maximum stress levels used in the experiments vary from $1\% < B_r < 5\%$, which are relatively low and make it difficult to assess the full capabilities of the breakage-dependent constitutive model. Anyhow, the performance of the model is clearly satisfactory.

Table 3
Model parameters.

Group	Parameter	Value
Elastic parameters	K_o	80
	v	0.25
	n	0.8
Plastic parameters	p_{m0}(MPa)	0.007
	M_p	1.2
	λ	0.0057
Particle breakage	a(MPa)	120
	c_0	0.34
	m	0.3
	ψ_0 (MPa)	70
Creep	t_{ref}(min)	0.1
	d	0.37

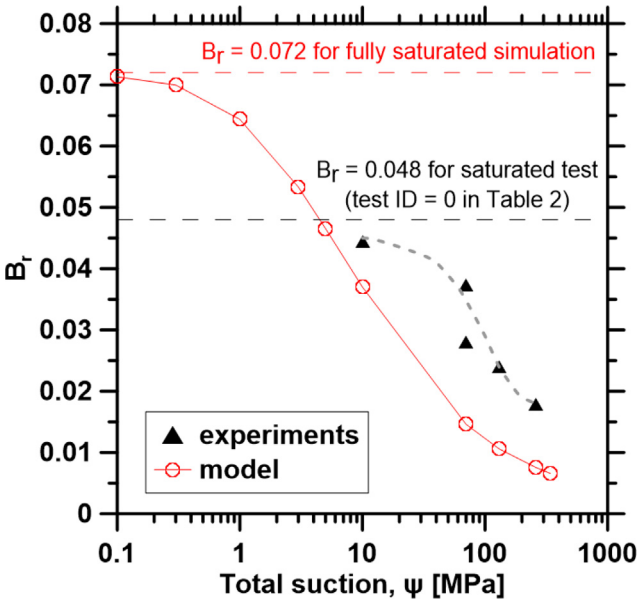

Fig. 20. Model estimates for B_r.

Whereas the experimental data reported here includes only oedometric compression, results presented above are promising and open new perspectives for modelling the effect of total suction on time-dependent behaviour of crushable granular materials. Further research work will be required to calibrate the model using experimental results obtained for different mechanical and hydraulic paths aimed at applying the model to simulate boundary value problems.

5. Conclusions

Several authors have hypothesized that Stress Corrosion Cracking phenomenon is responsible of delayed fragmentation in stressed rock particles. Thus, corrosion in intra-particle microcracks slowly develops, producing creep settlements of crushable granular materials. To further study this issue and support the development of a modelling approach, this paper has presented experimental evidence on the dependency of compressibility and crushing behaviour of sandy sized samples of crushed rock on total suction (or relative humidity). The results of oedometric tests over a large range of total suction from 0 to 340 MPa confirm that both compressibility and creep strains increase with stress and humidity. The analyses of compressibility indexes, particle size distributions before and after compression tests, and time-settlement curves, are in agreement with the hypothesis of the Stress Corrosion Cracking concept. Moreover, comparing tests at different total suctions, it is observed that delayed deformation rises his portion in total deformation when

humidity increases, which confirms few data previously reported on this issue.

Two new equations have been incorporated into the model developed by Ovalle and Hicher (2020) to consider the effect of total suction on creep behaviour. These correspond to: (i) a total suction-dependent equation governing the onset of particle breakage, and (ii) a time-dependent equation for the rate of breakage-hardening. The model was calibrated against a reduced set of experimental data and then used to simulate the laboratory tests. Model simulations capture well the trends of the material behaviour and the effect of total suction on compressibility, particle breakage and time-dependent behaviour under one-dimensional testing conditions. However, the model seems to underestimate the material response at high values of total suction, which indicates that further research is needed to enhance calibrations against tests following more diverse stress paths and at higher plastic work levels (i.e. higher stress). Perspectives of this work are validating the model for a general 3D stress state, using empirical data on diverse crushable materials presenting high sensitivity to humidity.

Acknowledgements

This research work benefitted from the financial support of CONICYT Chile through project FONDECYT 11150084, the Natural Sciences and Engineering Research Council of Canada (NSERC) [funding reference number RGPIN-2019-06118], the *Fonds de recherche du Québec - Nature et technologies* (FRQNT) through *Programme de recherche en partenariat sur le développement durable du secteur minier-II* [funding reference number 2020-MN-281267] and the industrial partners of the Research Institute on Mines and the Environment (RIME) UQAT-Polytechnique.

References

Alonso, E.E., Olivella, S., Pinyol, N.M., 2005. A review of Beliche Dam. Géotechnique 55 (4), 267–285.

Alonso, E.E., Romero, E.E., Ortega, E., 2016. Yielding of rockfill in relative humidity-controlled triaxial experiments. Acta Geotech. 11 (3), 455–477.

Andò, E., Dijkstra, J., Roubin, E., Dano, C., Boller, E., 2019. A peek into the origin of creep in sand. Granular Matter 21 (1). https://doi.org/10.1007/s10035-018-0863-5.

Atkinson, B.K., 1984. Subcritical crack growth in geological materials. J. Geophys. Res. 89 (B6), 4077–4114.

Atkinson, B.K., Meredith, P.G., 1987. The theory of subcritical crack growth with applications to minerals and rocks. In: Atkinson, B.K. (Ed.), Fracture mechanics of rock. Academic Press, London, pp. 111–166.

Bauer, E., 2009. Hypoplastic modelling of moisture-sensitive weathered rockfill materials. Acta Geotech. 4, 261–272.

Blatz, J.A., Cui, Y.-J., Oldecop, L., 2008. Vapour equilibrium and osmotic technique for suction control. Geotech. Geol. Eng. 26 (6), 661–673.

Brzesowsky, R., Hangx, S., Brantut, N., Spiers, C., 2014. Compaction creep of sands due to time dependent grain failure: effects of chemical environment, applied stress, and grain size. J. Geophys. Res. Solid Earth 119, 7521–7541.

Chávez, C., Alonso, E.E., 2003. A constitutive model for crushed granular aggregates which includes suction effects. Soils Found. 43 (4), 215–227.

Chen, W.-B., Liu, K., Yin, Z.-Y., Yin, J.-H., 2020. Crushing and flooding effects on one-dimensional time-dependent behaviors of a granular soil. Int. J. Geomech. 20 (2), 04019156. https://doi.org/10.1061/(ASCE)GM.1943-5622.0001560.

Coop, M.R., Sorensen, K.K., Bodas Freitas, T., Georgoutsos, G., 2004. Particle breakage during shearing of a carbonate sand. Géotechnique 54 (3), 157–163.

Dano, C., Ovalle, C., Yin, Z., Daouadji, A., Hicher, P.-Y., 2018. Behavior of granular materials affected by grain breakage. In: Nicot, F., Millet, O. (Eds.), Advances in Multi-Physics and Multi-Scale Couplings in Geo-Environmental Mechanics, first ed. ISTE Press, pp. 95–132.

Daouadji, A., Hicher, P.-Y., Rahma, A., 2001. An elastoplastic model for granular materials taking into account grain breakage. Eur. J. Mech. A. Solids 20 (1), 113–137.

Decagon Devices, Inc., 2018. WP4C Water Dewpoint Potentiometer. Operator's Manual Version April 2018. Decagon Devices, Inc., Pullman, USA (www.decagon.com)..

Einav, Itai, 2007. Breakage mechanics- Part I: Theory. J. Mech. Phys. Solids 55 (6), 1274–1297.

Fredlund, D.G., Rahardjo, H., 1993. Soil Mechanics for Unsaturated Soils. John Wiley & Sons, Inc., New York, NY, USA.

Freiman, S.W., 1984. Effects of chemical environments on slow crack growth in glasses and ceramics. J. Geophys. Res. 89 (B6), 4072–4076.

Fu, Zhongzhi, Chen, Shengshui, Zhong, Qiming, Zhang, Yijiang, 2019. Modeling interaction between loading-induced and creep strains of rockfill materials using a hardening elastoplastic constitutive model. Can. Geotech. J. 56 (10), 1380–1394.

Indraratna, B., Salim, W., Rujikiatkamjorn, C., 2011. Advanced Rail Geotechnology-Ballasted Track. CRS Press, Boca Raton, FL, USA.

Jacinto, A.C., Villar, M.V., Gómez-Espina, R., Ledesma, A., 2009. Adaptation of the van Genuchten expression to the effects of temperature and density for compacted bentonites. Appl. Clay Sci. 42 (3-4), 575–582.

Kikumoto, Mamoru, Wood, David Muir, Russell, Adrian, 2010. Particle crushing and deformation behaviour. Soils Found. 50 (4), 547–563.

Lade, Poul V., Karimpour, Hamid, 2010. Static fatigue controls particle crushing and time effects in granular materials. Soil Found. 50 (5), 573–583.

Lambe, T.W., Whitman, R.V., 1969. Soil Mechanics. John Wiley & Sons, New York, USA, p. 553 pages..

Lee, I., Coop, M., 1995. The intrinsic behaviour of a decomposed granite soil. Géotechnique 45 (1), 117–130.

Lee, Kenneth L, Farhoomand, Iraj, 1967. Compressibility and crushing of granular soil in anisotropic triaxial compression. Can. Geotech. J. 4 (1), 68–86.

Leung, C.F., Lee, F.H., Yet, N.S., 2011. The role of particle breakage in pile creep in sand. Can. Geotech. J. 33 (6), 888–898.

Main, I., Meredith, P.G., 1991. Stress corrosion constitutive laws as a possible mechanism of intermediate-term and short-term seismic quiescence. Geophys. J. Int. 107, 363–372.

Marsal, R., 1973. Mechanical properties of rockfill dams. In: Hirschfeld, R., Poulos, S. (Eds.), Embankment-dam engineering: Casagrande Volume. Wiley, New York, NY, USA.

Mesri, G., Castro, A., 1987. Cα/Cc concept and K0 during secondary compression. J. Geotech. Eng. 113 (3), 230–247.

Mesri, Gholamreza, Godlewski, Paul M., 1977. Time- and Stress-Compressibility Interrelationship. J. Geotech. Eng. Div. ASCE 103 (5), 417–430.

Mesri, Gholamreza, Vardhanabhuti, Barames, 2009. Compression of granular materials. Can. Geotech. J. 46 (4), 369–392.

Nakata, Yukio, Hyodo, Masayuki, Hyde, Adrian F.L., Kato, Yoshinori, Murata, Hidekazu, 2001. Microscopic particle crushing of sand subjected to high pressure one-dimensional compression. Soils Found. 41 (1), 69–82.

Nobari, E., Duncan, J., 1972. Effect of reservoir filling on stresses and movements in earth and rockfill dams. International Report N°.TE-72-1, University of California..

Oldecop, L., Alonso, E., 2001. A model for rockfill compressibility. Géotechnique 51 (2), 127–139.

Oldecop, L., Alonso, E., 2004. Testing rockfill under relative humidity control. Geotech. Test. J. 27 (3), 269–278.

Oldecop, L., Alonso, E., 2007. Theoretical investigation of the time dependent behaviour of rockfill. Géotechnique 57 (3), 289–301.

Osses, R., Pineda, J., Ovalle, C., Linero, S., Fityus, S., 2019. Particle size effects on the water retention properties of colluvial sediments. In: 7th Asia-Pacific Conference on Unsaturated Soils. August 23∼25, 2019, Nagoya, Japan. Japanese Geotechnical Society Special Publication 7 (2), 335–339..

Ovalle, C., 2018. Role of particle breakage in primary and secondary compression of wet and dry sand. Géotech. Lett. 8 (2), 161–164.

Ovalle, Carlos, Dano, Christophe, Hicher, Pierre-Yves, 2013. Experimental data highlighting the role of surface fracture energy in quasi-static confined comminution. Int. J. Fract. 182 (1), 123–130.

Ovalle, Carlos, Dano, Christophe, Hicher, Pierre-Yves, Cisternas, Mónica, 2015. Experimental framework for evaluating the mechanical behavior of dry and wet crushable granular materials based on the particle breakage ratio. Can. Geotech. J. 52 (5), 587–598.

Ovalle, Carlos, Hicher, Pierre-Yves, 2020. Modeling the effect of wetting on the mechanical behavior of crushable granular materials. Geosci. Front. 11 (2), 487–494.

Ovalle, C., Dano, C., 2020. Effects of particle size–strength and size–shape correlations on parallel grading scaling. Géotech. Lett. 10 (2), 1–7. https://doi.org/10.1680/jgele.19.00095.

Parkin, A.K., 1991. Creep of rockfill. In: Maranha das Neves, E. (Ed.), Advances in Rockfill Structures. Springer, Dordrecht, The Netherlands, pp. 221–237.

Richart, F.E., Hall, J.R., Woods, R.D., 1970. Vibrations of soils and foundations. International series in theoretical and applied mechanics. Prentice-Hall, Englewood Cliffs, NJ, USA.

Romero, E., 2001. Controlled-suction techniques. In: Gehling, W.Y.Y., Schnaid, F. (Eds.) Proc. 4° Simpósio Brasileiro de Solos Nâo Saturados ÑSAT'2001. Porto Alegre, Brasil, pp. 535–542..

Scholz, C.H., 1968. Mechanism of creep in brittle rock. J. Geophys. Res. 73 (10), 3295–3302.

Schanz, T., Vermeer, P., 1998. On the stiffness of sand. In: Jardine, R.J. (Ed.), Pre-failure deformation behaviour of geomaterials. Institution of Civil Engineers, London, pp. 383–473.

Sohn, Changbum, Buscarnera, Giuseppe, 2019. Measurement and simulation of comminution rate in granular materials subjected to creep tests. Granular Matter 21 (3). https://doi.org/10.1007/s10035-019-0912-8.

Sowers, G., Williams, R., Wallace, T., 1965. Compressibility of broken rock and the settlement of rockfills. In: Proc. 6th ICSMFE, pp. 561–565..

Suwal, L., Kuwano, R., 2013. Statically and dynamically measured poisson's ratio of granular soils on triaxial laboratory specimens. Geotech. Test. J. 36 (4), 493–505.

Takei, Masataka, Kusakabe, Osamu, Hayashi, Taketo, 2001. Time-dependent behavior of crushable materials in onedimensional compression tests. Soils Found. 41 (1), 97–121.

Turcotte, D., 1986. Fractals and fragmentation. J. Geophys. Res. 91 (B2), 1921–1926.

West, T.R., 1995. Geology Applied to Engineering, first ed. Prentice-Hall, Upper Saddle River, New Jersey, USA, p. 560.

Xu, Qing, Orpe, Ashish V., Kudrolli, Arshad, 2007. Lubrication effects on the flow of wet granular materials. Phys. Rev. E 76 (3). https://doi.org/10.1103/PhysRevE.76.031302.

Yin, Z.-Y., Hicher, P.-Y., Dano, C., Jin, Y.-F., 2017. Modeling mechanical behavior of very coarse granular materials. J. Eng. Mech. 143, 1.

Zhang, Y.D., Buscarnera, G., 2017. A rate-dependent breakage model based on the kinetics of crack growth at the grain scale. Géotechnique 67 (11), 953–967.